A structural mechanism for directing inverse agonism of PPARγ

Richard Brust[1], Jinsai Shang[1], Jakob Fuhrmann[1], Jared Bass[1], Andrew Cano[1,3], Zahra Heidari[4,5], Ian M. Chrisman[4,5], Anne-Laure Blayo[2], Patrick R. Griffin[1,2], Theodore M. Kamenecka[2], Travis S. Hughes[4,5], and Douglas J. Kojetin[1,2,*]

[1]Department of Integrative Structural and Computational Biology, [2]Department of Molecular Medicine, [3]TSRI High School Student Summer Internship Program, The Scripps Research Institute, Scripps Florida, Jupiter, Florida 33458, USA

[4]Center for Biomolecular Structure and Dynamics, [5]Department of Biomedical and Pharmaceutical Sciences, University of Montana, Missoula, Montana 59812, USA

*Correspondence should be addressed to D.J.K.: E-mail: dkojetin@scripps.edu

Abstract

Small chemical modifications can have significant effects on ligand efficacy and receptor activity, but the underlying structural mechanisms can be difficult to predict from static crystal structures alone. Here we show how a simple phenyl-to-pyridyl substitution between two common covalent orthosteric ligands targeting peroxisome proliferator-activated receptor gamma (PPARγ) converts a transcriptionally neutral antagonist (GW9662) into an inverse agonist (T0070907). X-ray crystallography, molecular dynamics simulations, and mutagenesis coupled to activity assays reveal a water-mediated hydrogen bond network linking the T0070907 pyridyl group to Arg288 that is essential for inverse agonism. NMR spectroscopy reveals that PPARγ exchanges between two long-lived conformations when bound to T0070907 but not GW9662, including a conformation that prepopulates a corepressor-bound state, priming PPARγ for high affinity corepressor binding. Our findings demonstrate that ligand engagement of Arg288 may provide new routes for developing PPARγ inverse agonist.

Introduction

The nuclear receptor peroxisome proliferator-activated receptor gamma (PPARγ) is a molecular target for insulin sensitizing drugs, including the thiazolidinedione (TZD) or glitazone class of antidiabetic drugs [1]. TZDs are full agonists of PPARγ that induce transcriptional activation resulting in the differentiation of multipotent mesenchymal stem cells (MSCs) into adipocytes or fat cells. Unfortunately, PPARγ agonists used as therapeutic agents in patients with type 2 diabetes mellitus (T2DM) display adverse side effects, including differentiation of bone tissue into fat resulting in brittle bone.

9   Although originally it was thought that full activation of PPARγ was required for
10   antidiabetic efficacy, recent studies have shown that antidiabetic PPARγ ligands can
11   span a wide range of efficacies—including full and partial agonists, antagonists, and
12   inverse agonists that have robust or mild activating, neutral, or repressive
13   transcriptional properties, respectively [2-5]. Importantly, repressive PPARγ modulators
14   decrease fat accumulation in bone and promote bone formation [5,6], and pharmacological
15   repression or antagonism of PPARγ is implicated in the treatment of obesity [7,8] and
16   cancer [9-11].

17   In order to determine how to promote all of the positive effects of
18   pharmacologically targeting PPARγ on antidiabetic efficacy, bone formation, anti-
19   obesity, and cancer treatment, we need to understand the structural mechanisms that
20   elicit PPARγ activation (agonism) and repression (inverse agonism). These distinct
21   pharmacological phenotypes of PPARγ ligands are dictated by ligand-dependent
22   recruitment of transcriptional coregulator proteins (coactivators and corepressors) to the
23   PPARγ ligand-binding domain (LBD). The LBD contains the orthosteric ligand-binding
24   pocket for endogenous ligands, which is also the binding site for most synthetic ligands,
25   and the activation function-2 (AF-2) coregulator binding surface. The AF-2 surface is
26   composed of three LBD structural elements: helix 3, helix 5, and the critical helix 12 that
27   dynamically moves between two or more conformations in the absence of ligand [12].

28   The structural mechanisms affording activation of PPARγ are well understood.
29   Agonists stabilize an active state of the AF-2 surface by forming hydrogen bonds with
30   residues near helix 12. Full agonists form a critical hydrogen bond with the phenolic side
31   chain of Y473 on helix 12, strengthen coactivator and weaken corepressor binding
32   affinities, respectively, which induces robust transcriptional activation [12-14]. Partial or
33   graded agonists do not hydrogen bond to Y473, but mildly stabilize helix 12 via
34   interactions with other regions of the ligand-binding pocket, resulting less pronounced
35   changes in coregulator affinity and transcriptional activation [13-15]. Neutral or passive
36   antagonists, which make unfavorable interactions with F282 on helix 3, do not stabilize
37   helix 12 and display negligible changes in activation [3]. These findings have established
38   the structural mechanisms for eliciting robust (agonist), weak (partial agonist), or no
39   (antagonist) transcriptional activation of PPARγ. An inverse agonist has a profile
40   opposite of an agonist, increasing the binding affinity of corepressors and decreasing the
41   binding affinity of coactivators resulting in transcriptional repression. However,
42   relatively few studies have explored the structural mechanisms by which ligands repress
43   PPARγ transcription [6,16], and it remains poorly understood how to design inverse
44   agonists.

45   Here we compare two commonly used covalent PPARγ ligands, GW9662 [17] and
46   T0070907 [18], which are referred to as antagonists not because of their effects on PPARγ
47   transcription, but because they covalently attach to C285 and physically block ligand
48   binding to the orthosteric ligand-binding pocket. Remarkably, despite differing only by
49   a simple methine (CH) to nitrogen substitution, T0070907 displays properties of an

50 inverse agonist compared to GW9662, which shows negligible effects on transcription [17-
51 19]. To understand the structural basis for these effects, we solved the crystal structure of
52 T0070907-bound PPARγ, which revealed no major overall structural differences
53 compared to a crystal structure of GW9662-bound PPARγ that would explain the
54 difference in efficacy. However, detailed structural analysis revealed a water-mediated
55 hydrogen bond network that uniquely links R288 to the T0070907 pyridyl group—an
56 interaction that cannot occur with GW9662, which lacks a hydrogen bond acceptor.
57 NMR analysis revealed that T0070907-bound PPARγ populates two long-lived
58 structural conformations, one of which resembles the state populated by GW9662 and a
59 unique state that is similar to the corepressor-bound state, revealing a novel structural
60 mechanism for directing inverse agonism of PPARγ.

Results

T0070907 is an inverse agonist

63   GW9662 and T0070907 (**Figure 1A**) contain the same 2-chloro-5-nitro-*N*-
64 phenylbenzamide scaffold but differ by a simple atom change: a ring carbon in GW9662
65 phenyl group is replaced by a nitrogen-containing pyridyl group in T0070907. Using a
66 cell-based transcription assay (**Figure 1B**), we compared GW9662 and T0070907 to other
67 noncovalent activating and repressive PPARγ compounds (**Figure S1**). T0070907
68 repressed PPARγ transcription relative to DMSO treated cells, opposite to the agonist
69 rosiglitazone that increased PPARγ transcription, whereas GW9662 did not significantly
70 affect PPARγ transcription. The repressive efficacy of T0070907 is similar to or better
71 than SR10221 and SR2595, respectively, which are analogs of the neutral
72 antagonist/nonagonist parent compound SR1664 [6].

73   We next characterized how the ligands affect the recruitment of peptides derived
74 from the TRAP220 coactivator and the NCoR corepressor (**Figure 1C**), two coregulator
75 proteins that influence PPARγ-mediated transcription [20,21]. Compared to unliganded
76 PPARγ (**Figure 1D**), nonanoic acid (a natural PPARγ agonist)[22] and to a larger degree
77 rosiglitazone (a synthetic PPARγ agonist) increased the affinity of TRAP220 and
78 decreased the affinity of NCoR. Characteristic of an inverse agonist, T0070907 displayed
79 an opposite profile to the agonists: decreasing the affinity of TRAP220 and increasing the
80 affinity of NCoR. GW9662 displayed a similar trend as T0070907, though the changes in
81 coregulator affinity were subtler: the affinity for NCoR increased, but unlike T0070907
82 the affinity for TRAP220 did not change (weaken) appreciably. Interestingly, the
83 repressive compounds SR2595 and SR10221 have distinct profiles compared to
84 T0070907: characteristic of a direct antagonist, they decreased affinity for both TRAP220
85 and NCoR.

86   We were interested in the structural mechanism by which the seemingly minor
87 methine-to-nitrogen ligand substitution could switch a covalent neutral antagonist
88 (GW9662) into a covalent inverse agonist (T0070907). Noncovalent analogs of the PPARγ

89 agonist farglitazar [16] and the neutral antagonist/nonagonist SR1664 [6] were designed to

90 perturb the conformation of the helix 12/AF-2 surface. The farglitazar analogs contain

91 ligand extensions towards helix 12. SR2595 and SR10221 contain a tert-butyl extension

92 that perturbed the conformation of F282 on helix 3 (**Figure 1E**) located within the

93 orthosteric pocket near the loop preceding helix 12, a region we refer to as the helix 12

94 subpocket. We previously showed that the F282/AF-2 steric clash caused by SR2595 and

95 SR10221 binding increases the dynamics of helix 3, which is part of the AF-2 surface,

96 thereby reducing the basal activity of PPARγ [6]. Our coregulator recruitment data show

97 this AF-2 clash affords a direct antagonist profile for SR2595 and SR10221 that leads to

98 transcriptional repression (**Figure 1B–D**). However, the phenyl (GW9662) to pyridyl

99 (T0070907) change is distant from F282, the helix 12 subpocket, or the AF-2 surface

100 (**Figure 1E**), suggesting the inverse agonist profile of T0070907 may originate from a

101 unique structural mechanism.

102 *A pyridyl-water hydrogen bond network unique to T0070907*

103 To gain structural insight into the mechanism of action, we solved the crystal

104 structure of T0070907 covalently bound to PPARγ to a resolution of 2.26 Å (PDB code

105 6C1I**; Table S1**) and compared our structure to an available crystal structure of GW9662-

106 bound PPARγ (PDB code 3B0R). In both cases, PPARγ crystallized in the same space

107 group and contained a dimer in the asymmetric unit with the expected alpha helical

108 sandwich fold (**Figure 2A**). Structural superposition revealed nearly identical backbone

109 conformations between the two structures (Cα r.m.s.d.: overall, 1.7 Å; chain A only,

110 1.34 Å; chain B only, 1.73 Å). In each of the structures, chain A adopts an "active"

111 conformation with helix 12 docked into the activation function-2 (AF-2) surface, whereas

112 helix 12 in chain B is distorted due to crystal packing interactions (**Figure S2**). Our

113 crystals of T0070907-bound PPARγ were obtained by soaking the ligand into preformed

114 apo-protein crystals since our cocrystallization attempts failed. Strong electron density

115 was observed for T0070907 in chain B and lower, less defined electron density in chain

116 A.

117 Focusing on the pyridyl ring of T0070907, a water-mediated hydrogen bond

118 network connects the pyridyl nitrogen to the Nε atom in the R288 side-chain

119 (**Figure 2B**). Furthermore, the guanidinyl side chain of R288 forms a bipartite hydrogen

120 bond with the side chain of E295. In contrast, in the GW9662-bound structure the

121 hydrogen bond network is not extensive due the lack of a hydrogen bond acceptor in the

122 phenyl ring of GW9662 (**Figure 2C**). To confirm the stability of the network observed in

123 the crystal structures, we performed molecular dynamics simulations of T0070907- and

124 GW9662-bound PPARγ ranging from 4–26 microseconds in length (**Figure 2D**)

125 preserving the crystallized waters (xtal), as well as a model we generated of T0070907-

126 bound PPARγ from the GW9662-bound PPARγ crystal structure solvated without

127 crystallized waters (model). In the simulations, the pyridyl group of T0070907 was

128 hydrogen bonded to a water molecule for a significant fraction of the simulation (65–

129 95%), as was the water-bridged R288-T0070907 pyridyl (5–46%). In contrast, a direct

130 interaction between R288 and the pyridyl group of T0070907 not mediated by water was
131 lowly populated (<2%). A direct (4–64%) and water-bridged (3–61%) R288-E295
132 interaction was also confirmed. The extensive pyridyl-based water-mediated hydrogen
133 bond network is not possible to the hydrophobic phenyl group of GW9662, revealing a
134 unique chemical feature in T0070907 that could confer inverse agonism.

135 *The pyridyl-water network is essential for inverse agonism*

136 To test the functional role of the pyridyl-water hydrogen bond network observed
137 in our T0070907-bound crystal structure, we generated variants of PPARγ by mutating
138 residues that we predicted would maintain or break the pyridyl-water network. We
139 hypothesized that mutation of R288 to a different positively charged residue (R288K)
140 would maintain the pyridyl-water network, whereas mutation to a hydrophobic residue
141 (R288A or R288L) would break the pyridyl-water network. If the hydrogen bond
142 network is important for inverse agonism, we hypothesized that breaking this network
143 via hydrophobic R288 mutations would afford a similar functional efficacy profile for
144 both T0070907 and GW9662. We also generated a E295A mutation to test the importance
145 of the bipartite hydrogen bond between R288 and E295. These mutations did not affect
146 the structural integrity or stability of the PPARγ LBD as assessed by circular dichroism
147 (CD) spectroscopy (**Figure S3**).

148 Using a cell-based transcription assay, we tested the combined effect of the
149 mutants and covalent ligands on PPARγ cellular activation (**Figure 3A**). Wild-type
150 PPARγ and the R288K mutant showed a similar profile, where cells treated with
151 T0070907 showed decreased PPARγ transcription compared to DMSO or GW9662
152 treatment. In contrast, T0070907 did not decrease transcription for the R288A or R288L
153 mutants, indicating the R288-mediated pyridyl-water network is responsible for the
154 transcriptional repression conferred by T0070907. The E295A mutant maintained the
155 cellular efficacy preference of T0070907 over GW9662, indicating that bipartite hydrogen
156 bond is not a major contributor to stabilizing the repressive activity, though both
157 GW9662 and T0070907 showed lower activity compared to wild-type PPARγ.

158 We next tested the effect of the mutants on coregulator recruitment by
159 determining binding affinities for the TRAP220 (**Figure 3B**) and NCoR (**Figure 3C**)
160 peptides for wild-type PPARγ LBD and the mutant variants with or without
161 pretreatment with GW9662 or T0070907. Consistent with the cell-based transcription
162 assay, the R288K and E295A mutants maintained the inverse agonist coregulator
163 binding profile of T0070907 and rank ordering. In contrast, the R288A and R288L
164 mutants showed similar affinity for TRAP220 and NCoR when covalently bound to
165 T0070907 or GW9662. This indicates the pyridyl-water network directs the inverse
166 agonism profile of T0070907, the lack of which results in a neutral antagonist profile.

167 To more robustly compare how the wild-type and mutant PPARγ variants
168 performed in the above assays, we performed a version of the "web of efficacy" analysis

169   used in the G-protein coupled receptor (GPCR) field to study ligand signaling bias [23,24].
170   We plotted the multivariate data on a radar chart with axes corresponding to each of the
171   assays whereby conditions with the most efficacious (i.e., that are biased towards)
172   inverse agonism properties populate the outer ring of the radar chart, and less favorable
173   or efficacious conditions populate the center (**Figure 3F**). The analysis clearly shows that
174   T0070907 selects more efficacious inverse agonism functions only for wild-type PPARγ
175   and the R288K mutant variant (**Figure 3G**). This dramatic result reveals that R288-
176   mediated pyridyl-water network directs inverse agonism conferred by T0070907.

177   *T0070907-bound PPARγ exchanges between two long-lived conformations*

178   Despite the different inverse agonist and neutral antagonist profiles of T0070907
179   and GW9662, the pyridyl-water network is the primary structural difference observed in
180   the crystal structures. In principle, there should be structural changes in the AF-2
181   coregulator interaction surface to account for the different pharmacological profiles.
182   Notably, however, the conformation of the AF-2 surface, which includes helix 12, is
183   influenced by crystal contacts (**Figure S2**). Furthermore, structural superposition of
184   PPARγ crystal structures bound to pharmacologically distinct ligands shows no major
185   structural changes that explain their different activities [25]. However, NMR studies have
186   shown that the orthosteric pocket and helix 12 are dynamic on the microsecond-to-
187   millisecond (μs-ms) time scale in the ligand-free/apo-form, which results in very broad
188   or unobserved NMR peaks for residues in helix 12 and within the orthosteric pocket and
189   surrounding regions [6,13]. Binding of a noncovalent full agonist stabilizes the helix 12/AF-
190   2 surface resulting in the appearance of NMR peaks that were missing in the apo-form,
191   whereas noncovalent partial agonists, neutral antagonists, and inverse agonists do not
192   stabilize helix 12 [6,13,25].

193   We used NMR spectroscopy to assess the impact of T0070907 and GW9662 on
194   the dynamics of the PPARγ LBD. NMR data of apo-PPARγ are similar to PPARγ
195   covalently bound to GW9662 with widespread μs-ms dynamics in the ligand-binding
196   pocket and helix 12/AF-2 surface [26]. In remarkable contrast, T0070907-bound PPARγ
197   showed a wide-spread stabilization of μs-ms dynamics, evident by the appearance of
198   peaks in 2D [^{1}H,^{15}N]-transverse relaxation optimized spectroscopy-heteronuclear single
199   quantum coherence (TROSY-HSQC) NMR spectra relative to GW9662-bound PPARγ
200   (**Figure 4A**). This includes well-resolved T0070907-bound NMR peaks corresponding to
201   residues located in close proximity to the T0070907 R288-mediated pyridyl-water
202   network (**Figure 4B**) in the β-sheet (V248, G344, G346), helix 3 (I279, G284) and the
203   adjacent helix 7 (G361). Furthermore, an NMR peak V322 on helix 5 within the AF-2
204   surface also appears, indicating stabilization of the AF-2 surface. The T0070907-bound
205   crystal structure shows a larger network of water-mediated hydrogen bonds, which
206   form a molecular hub linking the pyridyl-water network to the the β-sheet (via backbone
207   hydrogen bonds to I341 and E343) and helix 5 (via backbone hydrogen bond to I326).

208   Temperature-dependent NMR studies (**Figure 4C**) further revealed a number of
209 PPARγ residues experience peak doubling when bound to T0070907, but not when
210 bound to GW9662, including G399 located near the AF-2 surface (**Figure 4B**). Peak
211 doubling indicates the presence of two long-lived T0070907-bound structural
212 conformations in slow exchange on the NMR time scale, where the difference in
213 chemical shift between the two states (Δv, in Hz) is much greater than the exchange rate
214 (k_{ex}) between conformations on the order of milliseconds-to-seconds (ms–s) [27]. Thus, the
215 increase in NMR peaks when PPARγ is bound to T0070907 is not only due to
216 stabilization of μs-ms dynamics but also the presence of two long-lived structural
217 conformations.

218   ZZ-exchange NMR experiments (also called EXSY, or exchange spectroscopy)
219 enable detection of the interconversion between long-lived structural states via transfer
220 of the ^{1}H chemical shift of one state to the other when $k_{ex} \approx$ 0.2–100 s^{-1} and $k_{ex} \gg \Delta v$.
221 Exchange crosspeaks for G399, which shows well dispersed peak doubling, were
222 observed at 37°C but not at 25°C (**Figure 4D**), indicating the exchange between the two
223 conformations is too slow to be measured at room temperature (k_{ex} < 0.2/s). To determine
224 an exchange rate, we performed ZZ-exchange experiments with varying exchange
225 delays at 37°C and fit the data to a two-state interconversion model (**Figure 4E**), which
226 provided an exchange rate of ~2.1/s between the upfield shifted state (P_A = 37%; $k_{A \rightarrow B}$ =
227 0.8/s) and downfield shifted state (P_B = 63%; $k_{B \rightarrow A}$ = 1.3/s). Notable peak doubling, many
228 of which show well dispersed exchange crosspeaks, is widespread through the PPARγ
229 LBD (**Figure S4A**), though in most cases spectral overlap did not permit fitting of the
230 data to extract an exchange rate. However, residues with notable peak doubling
231 comprise distant structural regions that are also connected via the aforementioned
232 extended pyridyl-water network (**Figure 4B**), including the β-sheet (G338) and helix 6
233 (R350, S355, L356) within the ligand-binding pocket; a surface comprising helix 2a
234 (R234) and the C-terminal region of helix 7 and the loop connecting helix 7 and 8 (K373,
235 N375, E378, D380); helix 3 near the AF-2 surface (I303); and the loop connecting helix 8
236 and 9 near the AF-2 surface (S394), which also includes G399. In total, the NMR analysis
237 revealed that T0070907-bound PPARγ undergoes a global conformational change
238 between two long-lived structural conformations.

239 *T0070907 populates a mutual conformation with GW9662 and a unique conformation*

240   G399 is an ideal NMR observable probe that is sensitive to the conformation of
241 the AF-2 surface: it is structurally proximal and linked to the AF-2 surface through
242 water-mediated hydrogen bonds to N312 and D311 on helix 5, but does not directly
243 interact with a bound coregulator peptide (**Figure 5A**). Strikingly, for G399 and the other
244 residues that showed peak doubling in the ZZ exchange analysis, we found that the
245 backbone amide chemical shifts of one of the two peaks observed for T0070907-bound
246 PPARγ are similar to the single peak observed for GW9662-bound PPARγ (**Figure 5B**
247 **and Figure S4B**). This indicates that one of the long-lived T0070907-bound
248 conformations is structurally similar to GW9662-bound PPARγ, which below we refer to

249 as the mutual conformation, and the other conformation is uniquely populated only
250 when bound to T0070907.

251 We also assessed the conformational state of helix 12 directly using ^{19}F NMR
252 (**Figure 5C**) by attaching the ^{19}F NMR-detectible probe 3-bromo-1,1,1-trifluoroacetone
253 (BTFA) on K474 (**Figure 5A**). The ^{19}F spectral profile of GW9662-bound PPARγ revealed
254 two peaks corresponding to a major state (right peak; 78%) and minor state (left peak;
255 22%). T0070907-bound PPARγ also shows two peaks with chemical shift values similar
256 to GW9662-bound PPARγ, but the population magnitudes of the states are switched and
257 skewed towards the left peak. Strikingly, this helix 12/AF-2 surface ^{19}F NMR probe
258 showed the same relative population sizes observed in the G399/proxy to the AF-2
259 surface ZZ-exchange analysis (34% and 66%, respectively). The right peak abundantly
260 populated by GW9662 and moderately populated by T0070907 likely corresponds to the
261 mutual G399 conformation from the 2D NMR analysis. In contrast, the left ^{19}F NMR
262 peak likely corresponds to the unique G399 conformation; this peak is abundantly
263 populated by T0070907 but lowly populated by GW9662. The low abundance of this
264 peak when bound to GW9662 could explain in part why it was not detected by the 2D
265 NMR analysis, which has lower overall sensitivity of signal-to-noise compared to the ^{19}F
266 NMR analysis. However, the BTFA probe attached to helix 12 may also be sensitive to
267 larger structural changes, and thus chemical environments, compared to backbone
268 amide of G399.

269 *The unique T0070907 conformation prepopulates a corepressor-bound conformation*

270 We wondered whether the unique and mutual long-lived T0070907-bound
271 conformations would display similar or distinct coregulator interaction preferences. To
272 test this, we titrated the NCoR corepressor and TRAP220 coactivator peptides and
273 monitored their binding to ^{15}N-PPARγ LBD by NMR. Remarkably, titration of NCoR
274 corepressor peptide into T0070907-bound PPARγ (**Figure 5D,E**) resulted first in a
275 shifting of the unique G399 conformation (peak *B*) towards a similar chemical shifts
276 values and intensity, nearly saturating around 0.6 equiv NCoR, which is the
277 approximate population (P_B) of the state from the ZZ-exchange analysis. Only minor
278 changes in peak intensity were observed for the mutual peak (peak *A*) until the titration
279 reached 0.6 equiv NCoR peptide, at which point this peak decreased in intensity with a
280 concomitant increase in the intensity of the unique conformation peak that shifted to the
281 NCoR-bound conformation. This second transition (peptide free state $A \rightarrow$ NCoR bound
282 state) saturated at 1 equiv of NCoR peptide in slow exchange on the NMR time scale.
283 These results are consistent with our coregulator affinity data showing mid-nM affinity
284 for NCoR binding.

285 We next examined the effect of TRAP220 peptide binding to T0070907-bound
286 PPARγ (**Figure 5F,G**). In contrast to the NCoR results, the mutual conformation of G399
287 (state *A*) transitioned first to a peak with similar chemical shift values and intensity. This
288 first transition saturated at the first titration point (0.5 equiv), which is slightly larger

than the approximate population (P_A) of the state from the ZZ-exchange analysis. A second transition also occurred where the unique conformation (state *B*) showed a decrease in peak intensity, but only at TRAP220 amounts more than 0.5 equiv, which resulted in a concomitant increase in the intensity of the mutual peak that shifted to the TRAP220-bound peak. This second transition did not saturate until 4 equiv of TRAP220 was added, indicating that the unique conformation displays much weaker affinity for TRAP220 relative to the mutual conformation. Notably, the same coregulator binding trends for the other residues with peak doubling, where NCoR binding shifts the peak populations towards the unique state *B* (**Figure S4C**) and TRAP220 binding shifts the peak populations towards the mutual state *A* (**Figure S4D**).

Finally, we examined the binding of GW9662-bound PPARγ with NCoR (**Figure 5H**) and TRAP220 (**Figure 5I**). Interestingly, whereas NCoR or TRAP200 binding to T0070907-bound PPARγ consolidated the unique and mutual conformations into one peptide-bound conformation, NCoR binding to GW9662-bound PPARγ caused peak doubling of the single GW9662-bound G399 NMR peak towards chemical shift values similar to the NCoR- and TRAP220-bound form of T0070907-bound PPARγ. In contrast, TRAP220 binding only shifted the single GW9662-bound G399 peak towards the TRAP220-bound form of T0070907-bound PPARγ.

These dramatic results reveal that the two long-lived T0070907-bound conformations have different binding preferences for NCoR and TRAP220. The NMR chemical shit perturbation profiles reveal that the unique conformation has strong affinity for NCoR but weak affinity for TRAP220, whereas the mutual conformation has moderate affinity for NCoR and strong affinity for TRAP220. Moreover, the NMR chemical shifts of the unique and mutual T0070907-bound conformations in the absence of coregulator peptide are similar to the NCoR- and TRAP220-bound forms, respectively. This indicates that the unique and mutual T0070907-bound states prepopulate a corepressor-like and coactivator-like bound conformation that individually afford privileged high-affinity binding to NCoR and TRAP220, respectively. Furthermore, the chemical shift difference between the unique T0070907 conformation and NCoR-bound state (i.e., the degree of state *B* shifting) is much smaller than the mutual conformation and TRAP220-bound state (i.e., the degree of state *A* shifting). This indicates the corepressor-like conformation prepopulated by T0070907 is more similar to the corepressor-bound state than the coactivator-like conformation prepopulated by T0070907 is to the coactivator-bound state. In contrast, NCoR binding to GW9662-bound PPARγ introduces a "conformational frustration" within the AF-2 surface. In addition to not prepopulating the corepressor-bound conformation, the AF-2 surface of GW9662-bound PPARγ is found in both the corepressor- and coactivator-bound conformations upon binding NCoR—both of which could contribute to the neutral antagonism profile for GW9662 as opposed to the enhanced inverse agonism profile of T0070907 derived through prepopulation of conformational states that have high affinity for corepressor and low affinity for coactivator.

Discussion

Carbon (methine)-to-nitrogen ligand substitutions are known to have beneficial effects on pharmacological parameters [28], though it is difficult to predict how subtle changes in chemical structure impact switches in functional efficacy [29,30]. GW9662 and T0070907 are widely used as chemical tools due to their ability to covalently bind to PPARγ and inhibit ligand binding to the orthosteric ligand-binding pocket. Although it is generally acknowledged that these highly similar compounds display distinct PPARγ activity profiles, the molecular basis for their functional differences in efficacy has remained elusive. Our studies, which combine crystallography, molecular dynamics simulations, NMR spectroscopy, and mutagenesis coupled with biochemical and cellular assays, illuminate a novel structural mechanism affording the inverse agonism of T0070907. Our crystal structure of T0070907-bound PPARγ revealed a water-mediated hydrogen bond network linking the critical inverse agonist "switch" residue, R288, which is distal from the activation function-2 (AF-2) coregulator interaction surface, to the pyridyl group of T0070907. Our NMR analysis shows that T0070907-bound PPARγ, but not GW9662-bound PPARγ, slowly exchanges between two long-lived conformations. One of these conformations is shared with GW9662-bound PPARγ and similar to the coactivator-bound state. The other conformation is uniquely and abundantly populated by T0070907 and highly similar to the corepressor-bound state, thus affording higher affinity corepressor binding and inverse agonism for T0070907.

We demonstrated the importance of the pyridyl-water network in directing inverse agonism of PPARγ using mutagenesis coupled with functional assays. However, no major structural differences were observed in the crystal structures that explain their functional profiles. In contrast, our NMR data revealed clearly that T0070907-bound PPARγ, but not GW9662-bound PPARγ, exchanges between two long-lived conformations, one of which prepopulates a conformation similar to the corepressor-bound state. The active AF-2 conformation bound to a coactivator peptide has captured in numerous crystal structures of PPARγ and other nuclear receptors. Thus far, no structures have been reported for PPARγ bound to a corepressor peptide and, relative to coactivator-bound structures, a limited number of structures have been reported for corepressor-bound nuclear receptors [31]. However, from these studies it is known that the binding regions of coactivator and corepressor (NCoR and SMRT) peptides overlap. In the corepressor-bound structures, helix 12 is displaced from its "active" conformation and shows variability in its crystallized conformation, which may reflect a dynamic "inactive" conformational profile. Our NMR studies show that as a whole the AF-2 surface, using G399 as a proxy, is primed for high affinity binding to NCoR when PPARγ is bound to T0070907.

There are two main underlying conclusions from our NMR findings on T0070907-bound PPARγ. First, the crystallized AF-2 conformations do not likely represent the conformations of T0070907-bound PPARγ in solution, since crystal packing influence the position of helix 12. Our differential NMR analysis not only

371   revealed peak doubling for T0070907-bound PPARγ but also a stabilization of μs-ms

372   timescale dynamics relative to GW9662-bound PPARγ. Furthermore, using ^{19}F NMR we

373   showed that helix 12 dynamically exchanges between two long-lived conformations, one

374   of which is significantly populated only by T0070907. Second, we used molecular

375   dynamics simulations to verify the structural integrity of the pyridyl-water network.

376   However, given that the NMR-detected exchange rate between the two T0070907-bound

377   conformations is >1s, access to helix 12/AF-2 conformations that would be consistent

378   with our NMR data in molecular simulations is inaccessible with current standard

379   simulation approaches. Overall, our work shows that the combination of different but

380   complementary structural methods—crystallography, NMR, and molecular

381   simulations—provides the full picture of ligand mechanism of action, which as we

382   demonstrate here, involves a simultaneous prepopulation of long-lived conformational

383   states with distinct functions.

384   Our findings suggest a new means for pharmacologically directing

385   transcriptional repression via inverse agonism of PPARγ. The previous finding that

386   ligand engagement of, or hydrogen binding to, helix 12 via Y473 is critical for mediating

387   agonism transformed the way that PPARγ agonists were developed [32]. The AF-2 steric

388   clash mechanism of action for the repressive PPARγ compounds SR2595 and SR10221 [6,16]

389   shows a coregulator interaction profile consistent with a direct antagonist rather than an

390   inverse agonist. In contrast, our studies here indicate that ligand hydrogen bonding to

391   the guanidinyl side chain of R288, water-mediated or perhaps directly, may be a critical

392   mediator of inverse agonism. Repressive PPARγ modulators show promise for

393   improving the therapeutic index associated with anti-diabetic PPARγ ligands by

394   promoting bone formation rather than decreasing bone mass [5,6], which occurs with

395   agonists used clinically such as the TZDs. Furthermore, repression of PPARγ activity

396   affects fat mobilization and may be a means to therapeutically treat obesity and extend

397   lifespan [7], and T0070907 has demonstrated efficacy in cancer models [9-11]. Thus, our

398   findings should inspire future work to develop and characterize inverse agonists to

399   probe the repressive functions of PPARγ.

400   **Methods**

401   *Materials and reagents*

402   Human PPARγ LBD (residues 203–477 in isoform 1 numbering, which is

403   commonly used in published structural studies and thus throughout this manuscript; or

404   residues 231–505 in isoform 2 numbering) or mutant proteins were expressed in

405   *Escherichia coli* BL21(DE3) cells as TEV-cleavable hexahistidine-tagged fusion protein

406   using a pET46 plasmid as previously described [13,26]. The final storage buffer for samples

407   following size exclusion chromatography and subsequently frozen at -80 °C was 50 mM

408   potassium chloride (pH 7.4), 20 mM potassium phosphate, 5 mM TCEP, and 0.5 mM

409   EDTA. Covalent ligand treatment was performed overnight at 4 °C with a 2X molar

410   excess of compound dissolved in d_6-DMSO. Mammalian expression plasmids included

411 Gal4-PPARγ-hinge-LBD (residues 185-477 in isoform 1 numbering; 213-505 in isoform 2
412 numbering) inserted in pBIND plasmid; and full-length PPARγ (residues 1-505; isoform
413 2) inserted in pCMV6-XL4 plasmid. Mutant proteins were generated using site directed
414 mutagenesis of the aforementioned plasmids. GW9662, T0070907, and SR1664 were
415 obtained from Cayman Chemical; rosiglitazone was obtained from Tocris Bioscience and
416 Cayman Chemical; SR2595 and SR10221 were previously synthesized in house [6].
417 Peptides of LXXLL-containing motifs from TRAP220 (residues 638–656;
418 NTKNHPMLMNLLKDNPAQD) and NCoR (2256–2278;
419 DPASNLGLEDIIRKALMGSFDDK) containing a N-terminal FITC label with a six-
420 carbon linker (Ahx) and an amidated C-terminus for stability were synthesized by
421 LifeTein.

Cell-based transcriptional luciferase reporter assay

423 HEK293T cells were cultured in DMEM medium supplemented with 10% fetal
424 bovine serum (FBS) and 50 units ml^{-1} of penicillin, streptomycin, and glutamine. Cells
425 were grown to 90 % confluency and then seeded in 10 cm dishes at 4 million cells per
426 well. Cells were transfected using X-tremegene 9 (Roche) and Opti-MEM (Gibco) with
427 pCMV6 full-length PPARγ expression plasmid (4.5 μg) and 3xPPRE-lucifease reporter
428 pGL2 plasmid (4.5 μg) and incubated for 18 h; plasmids were obtained from P. Griffin
429 (Scripps) as used in previous studies. [3,6,13,26] Cells were transferred to white 384-well
430 plates (Thermo Fisher Scientific) at 10,000 cells/well in 20 μL and incubated for 4 hr.
431 Ligand (5 μM) or vehicle control was added (20 μL), cells incubated for 18 hr and
432 harvested for luciferase activity quantified using Britelite Plus (Perkin Elmer; 20 μL) on a
433 BioTek Synergy Neo multimode plate reader (Biotek). Data were analyzed using
434 GraphPad Prism (luciferase activity vs. ligand concentration) and fit to a sigmoidal dose
435 response curve.

Fluorescence polarization (FP) coregulator interaction assay

437 The assay was performed in black 384-well plates (Greiner) in assay buffer (see
438 above). His-PPARγ LBD was pre-incubated with or without a 2X molar excess of
439 covalent ligand overnight at 4 °C and diluted by serial dilution. Noncovalent
440 compounds were incubated with a constant concentration of 90 μM, equivalent to the
441 maximum protein concentration, to ensure full occupancy. FITC-labeled NCoR and
442 TRAP220 peptides were plated at a final concentration of 100 nM. Plates were incubated
443 for 2 hr at 4 °C and measured on a BioTek Synergy Neo multimode plate reader at
444 485 nm emission and 528 nm excitation wavelengths. Data were plotted using GraphPad
445 Prism and fit to one-site binding equation.

Crystallography

447 PPARγ LBD protein was concentrated to 10 mg/ml and buffer exchange into
448 phosphate buffer (20 mM KH$_2$PO$_4$/K$_2$HPO$_4$, pH 8, 50 mM KCl, 5 mM TCEP). Apo-

449 PPARγ crystals were obtained after 3–5 days at 22°C by sitting-drop vapor diffusion
450 against 50 μl of well solution using 96-well format crystallization plates. The
451 crystallization drops contain 1 μl of protein sample mixed with 1 μl of reservoir solution
452 containing 0.1 M MOPS, 0.8 M sodium citrate at pH 6.5. T0070907 was soaked into the
453 PPARγ apo-crystals drop by adding 1 μl of compound at a concentration of 1 mM
454 suspended in the same reservoir solution for 3 weeks. Crystals were cryoprotected by
455 immersion in mother liquor containing 12% glycerol and flash-cooled in liquid nitrogen
456 before data collection. Data collection was carried out at Beamlines 5.0.1 of BCSB at the
457 Advanced Light Source (Lawrence Berkeley National Laboratory). Data were processed,
458 integrated, and scaled with the programs Mosflm and Scala in CCP4 [34,35]. The structure
459 was solved by molecular replacement using the program Phaser [36] implemented in the
460 PHENIX package [37] and used previously published PPARγ LBD structure (PDB code:
461 1PRG) [38] as the search model. The structure was refined using PHENIX with several
462 cycles of interactive model rebuilding in COOT [39].

463 *Molecular dynamics simulations*

464 A crystal structure of GW9662-bound PPARγ (PDB code 3B0R) along with our
465 crystal structure T0070907 bound to PPARγ (PDB code 6C1I) were used to build initial
466 structures in all simulations in this study. Two models were generated using 3B0R
467 crystal structure. In the first model, chain A of 3B0R was used and GW9662 was
468 transformed to T0070907 by converting phenyl ring of GW9662 to the pyridine ring of
469 T0070907. The second 3B0R generated model was built using chain B conformation. In
470 addition, chain B of the T0070907 crystal structure was used for a third build. The
471 crystalized water molecules were kept in the models in which chain B conformations
472 were used. The Modeller [40] extension within UCSF Chimera [41] was used to fill in the
473 missing part of the protein in PDB files. The resulting structures were submitted to H++
474 server [42] to determine the protonation states of titratable residues at pH 7.4. AMBER
475 names were assigned to different protonation states of histidine using pdb4amber
476 provided in AmberTools 14 [3]). In order to parametrize T0070907 and GW9662, the C285
477 with covalently attached ligand was protonated and methyl caps were added, saved as a
478 separate PDB file using Chimera, and submitted to the R.E.D server [43] to calculate RESP
479 [44] charges. AMBER cysteine residue values were used for the RESP charges for the
480 cysteine backbone. The output mol2 file was used to generate the ac and prepin files
481 following a method in the tutorial (http://ambermd.org/tutorials/basic/tutorial5/).
482 Parmchk2 was used to create two force modification files from the prepin file, one that
483 used AMBER ff14SB [45] parameter database values and another that used general Amber
484 force field [46] (GAFF2) values, then Tleap was used to generate topology and coordinate
485 files. The ff14SB force field was used to describe the protein. The resulting structure
486 was solvated in a truncated octahedral box of TIP3P water molecules with the 10 Å
487 spacing between the protein and the boundary, neutralized with Na+ and K+ and
488 Cl⁻ ions were added to 50 mM. The system was minimized and equilibrated in nine steps
489 at 310 K with nonbonded cutoff of 8 Å. In the first step the heavy protein atoms were
490 restrained by a spring constant of 5 kcal/mol Å² for 2000 steps, followed by 15 ps

491 simulation under NVT conditions with shake, then two rounds of 2000 cycles of steepest
492 descent minimization with 2 and 0.1 kcal/mol $Å^2$ restraints were performed. After one
493 round without restraints, three rounds of simulations with shake were conducted for 5
494 ps, 10 ps and 10 ps under NPT conditions and restraints of 1, 0.5 and 0.5 kcal/mol $Å^2$ on
495 heavy atoms. Finally, an unrestrained NPT simulation was performed for 200 ps.
496 Production runs were carried out with hydrogen mass repartitioned [47] parameter files to
497 enable 4 fs time steps. Constant pressure replicate production runs were carried out with
498 independent randomized starting velocities. Pressure was controlled with a Monte Carlo
499 barostat and a pressure relaxation time (taup) of 2 ps. Temperature was kept constant at
500 310 K with Langevin dynamics utilizing a collision frequency (gamma_ln) of 3 ps^{-1}. The
501 particle mesh ewald method was used to calculate non-bonded atom interactions with a
502 cutoff (cut) of 8.0 Å. SHAKE [48] was used to allow longer time steps in addition to
503 hydrogen mass repartitioning. Analysis of trajectories was performed using cpptraj [49].
504 Hydrogen bond analysis was performed using dist = 3.5 Å and angle = 100° [50].

CD Spectroscopy

506 Protein samples pre-incubated with or without a 2X molar excess of covalent
507 ligand overnight at 4 °C were diluted to 10 μM in CD buffer (20 mM KPO_4 pH 7.4, 10
508 mM KCl, 1 mM TCEP, 10% glycerol) and measured on a JASCO J-815 CD spectrometer
509 by scanning from 190 nm to 300 nm at 20 °C or by increasing the temperature from 20 to
510 80 °C at 1 °C/min while monitoring the CD signal at 223 nm. Protein unfolding/melting
511 temperature (T_m) was determined by fitting the data to a thermal unfolding equation [51]
512 in GraphPad Prism.

NMR spectroscopy

514 2D [^{1}H,^{15}N]-TROSY HSQC NMR data of 200 μM ^{15}N-labeled PPARγ LBD, pre-
515 incubated with a 2X molar excess of covalent ligand overnight at 4 °C, were acquired at
516 298K (unless otherwise indicated) on a Bruker 700 MHz NMR instrument equipped with
517 a QCI cryoprobe in NMR buffer (50 mM potassium phosphate, 20 mM potassium
518 chloride, 1 mM TCEP, pH 7.4, 10% D_2O). For peptide titrations, peptides were dissolved
519 in NMR buffer. ZZ-exchange experiments were acquired at 298K or 310K on Bruker 700
520 or 800 MHz NMR instrument equipped with a QCI or TCI cryoprobe, respectively,
521 using exchange mixing times ranging from 0–2 s. Data were processed and analyzed
522 using Topspin 3.0 (Bruker Biospin) and NMRViewJ (OneMoon Scientific, Inc.) [52],
523 respectively. NMR chemical shift assignments previously described for ligand-bound
524 PPARγ [6,13,26] were assigned to the spectra for well resolved residues with consistent
525 NMR peak positions the presence of different ligands using the minimum chemical shift
526 perturbation procedure williamson[53]. ZZ exchange data were fit to an exchange model
527 for slow two-state interconversion [27,54] using a protocol described by, and a MATLAB
528 script provided by, Gustafson, et al. [55].

529   For ^{19}F NMR, PPARγ LBD K474C mutant protein was used to allow covalent
530   attachment of 3-bromo-1,1,1-trifluoroacetone (BTFA) helix 12 via K474C. Mass
531   spectrometry verified that GW9662 and T0070907 (2X molar excess) do not covalently
532   attach to K474C (using a K474C/C285S double mutant protein that is in capable of
533   covalent attachment to C285); using wild-type protein confirmed covalently attachment
534   to C285. Samples were first incubated with 2X GW9662 or T0070907, then incubated
535   with 2X BTFA, followed by buffer exchange into ^{19}F NMR buffer (25 mM MOPS, 25 mM
536   KCl, 1 mM EDTA, pH 7.4, 10% D_2O). 1D ^{19}F NMR data of 150 μM BTFA-labeled PPARγ
537   LBD bound to GW9662 or T0070907 were acquired at 298K on a Bruker 700 MHz NMR
538   instrument equipped with QCI-F cryoprobe. Chemical shifts were calibrated using an
539   internal separated KF reference in ^{19}F NMR buffer without TCEP contained in a coaxial
540   tube inserted into the NMR sample tube. KF was set to be —119.522 ppm, which is the
541   chemical shift of the KF signal with respect to the ^{19}F basic transmitter frequency for
542   instrument. 1D ^{19}F spectra were acquired utilizing the zgfhigqn.2 pulse program
543   provided in Topspin 3.5 (Bruker Biospin). Data were processed using Topspin and
544   deconvoluted with decon1d [56].

Acknowledgements

Author contributions

556   R.B. performed the cellular and biochemical assays. J.S. and J.F. performed
557   crystallography. J.S. and D.J.K. performed the 2D NMR experiments. I.M.C. and T.S.H.
558   performed the ^{19}F NMR experiments. Z.H., T.S.H, and D.J.K. performed the molecular
559   dynamics simulations. R.B., J.S., J.F., J.B., A.C., and I.M.C. performed mutagenesis
560   and/or purified proteins. A.-L.B., P.R.G., and T.M.K. supplied compounds. R.B. and D.K.
561   conceived the experiments and wrote the manuscript with input from all authors.
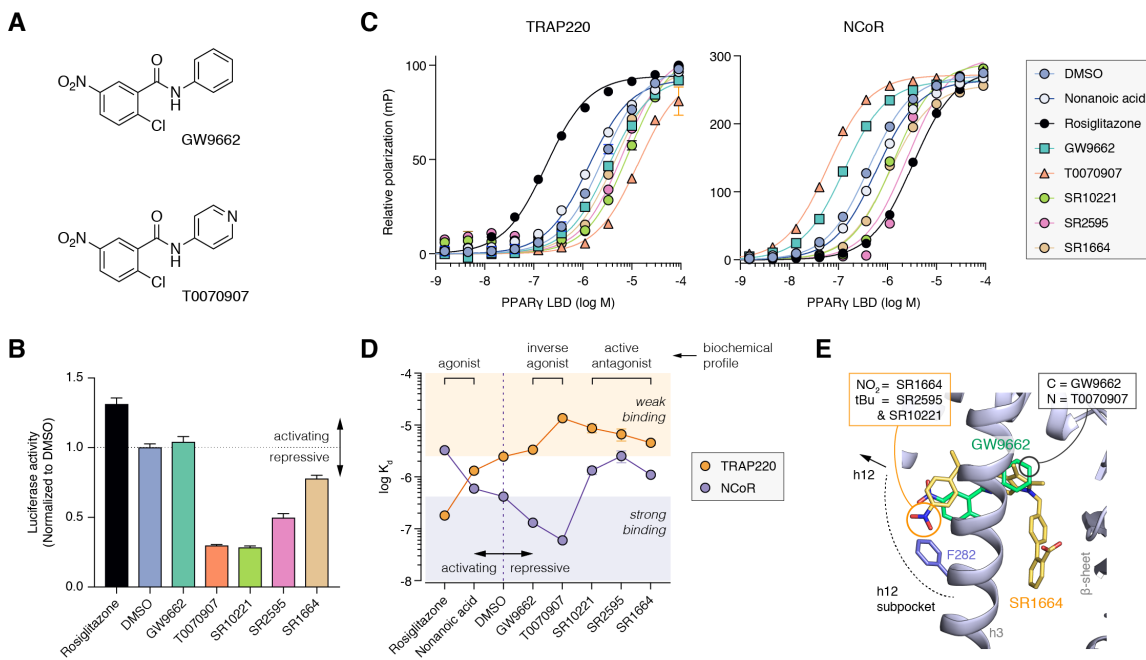
Figure 1. Differences in functional efficacy between GW9662, T0070907, and other synthetic PPARγ ligands.

(**A**) Chemical structures of GW9662 and T0070907.

(**B**) Cell-based luciferase transcriptional assay showing the effect of activating and repressive ligands (5 μM) on full-length PPARγ transcription in HEK293T cells.

(**C**) Fluorescence polarization coregulator interaction assay showing the effect of ligands on the interaction between the PPARγ LBD and peptides derived from the TRAP220 coactivator or NCoR corepressor.

(**D**) K_d values derived from the coregulator interaction assay. Dotted orange and purple lines note the DMSO/apo-PPARγ values. Orange and purple shaded areas note the affinity regions for an ideal inverse agonist (i.e., for weaker TRAP220 affinity, orange circles in the orange square; for higher NCoR affinity, purple circles in purple squares).

(**E**) Superposition of crystal structures of the PPARγ LBD bound to GW9662 (PDB code 3B0R; ligand in green, cartoon in blue) and SR1664 (PDB code 4R2U; ligand in yellow). The location of the simple substitution between GW9662 (methine) vs. T0070907 (nitrogen) is marked with a black circle, and the SR2595 and SR10221 tert-butyl extension within the helix 12 subpocket towards F282 (blue) from the SR1664 parent compound is marked with a yellow circle.
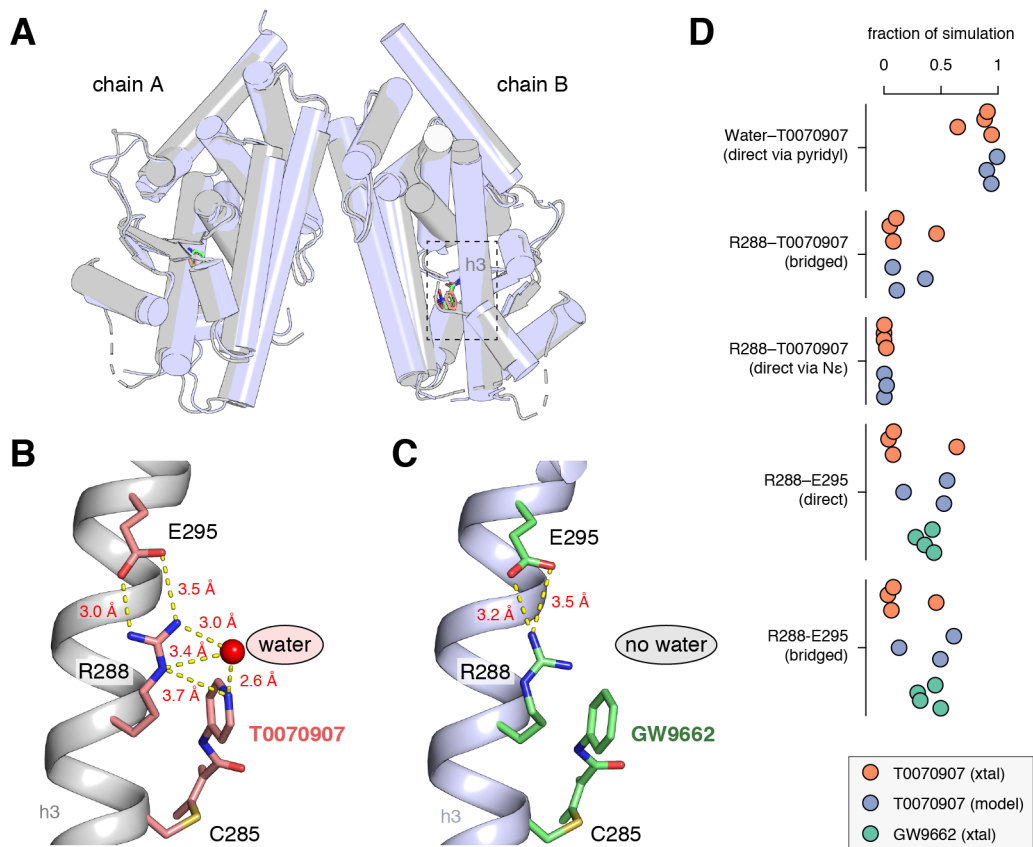
Figure 2. Crystal structure of T0070907-bound PPARγ LBD reveals a water-mediated pyridyl-protein hydrogen bond network.

(**A**) Overall structure of T0070907-bound PPARγ (PDB code 6C1I; grey) and overlay with GW9662-bound crystal structure (PDB code 3B0R; blue).

(**B**) A water-mediated hydrogen bond network in the T0070907-bound crystal structure (chain B is shown) links the pyridyl group in T0070907 to the R288 side chain, which forms a bipartite hydrogen bond with the E295 side chain.

(**C**) The GW9662-bound crystal structure (chain B is shown) lacks the R288-ligand hydrogen bond network but contains the R288-E295 hydrogen bond.

(**D**) Pyridyl-water network hydrogen bonds populated during molecular dynamics simulations for T0070907- and GW9662-bound structures starting from crystallized (xtal) and modeled (model) conformations.
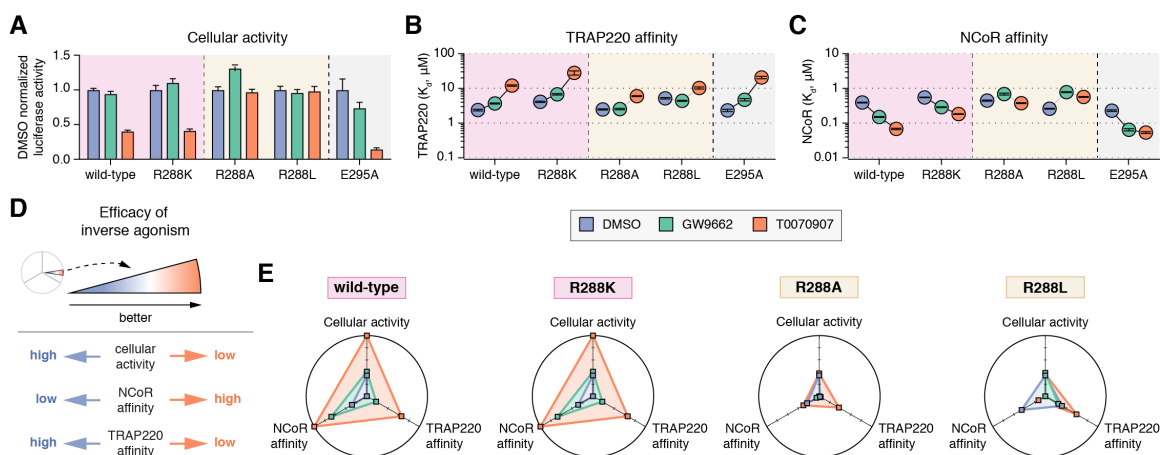
Figure 3. The R288-pyridyl interaction is essential for conferring inverse agonism.

(**A**) HEK293T cells transfected with full-length PPARγ expression plasmid along with a 3x-PPRE-luciferase reporter plasmid and treated with the indicated ligands (5 μM). Data plotted as the average and s.e.m. of six experimental replicates.

(**B,C**) Affinities determined from a fluorescence polarization assay of wild-type and mutant PPARγ LBDs preincubated with a covalent ligand (GW9662 or T0070907) or vehicle (DMSO) binding to FITC-labeled (**B**) TRAP220 or (**C**) NCoR. Data plotted as the K_d value and error from fitting data of two experimental replicates using a one site binding equation.

(**D**) Legend to the "web of efficacy" radar chart diagrams. Inverse agonism is associated with data points populating the periphery of the plots.

(**E**) Radar "web of efficacy" plots displaying assay data for wild-type PPARγ and mutant variants. Data normalized within the range of values for each assay (**A–C**).
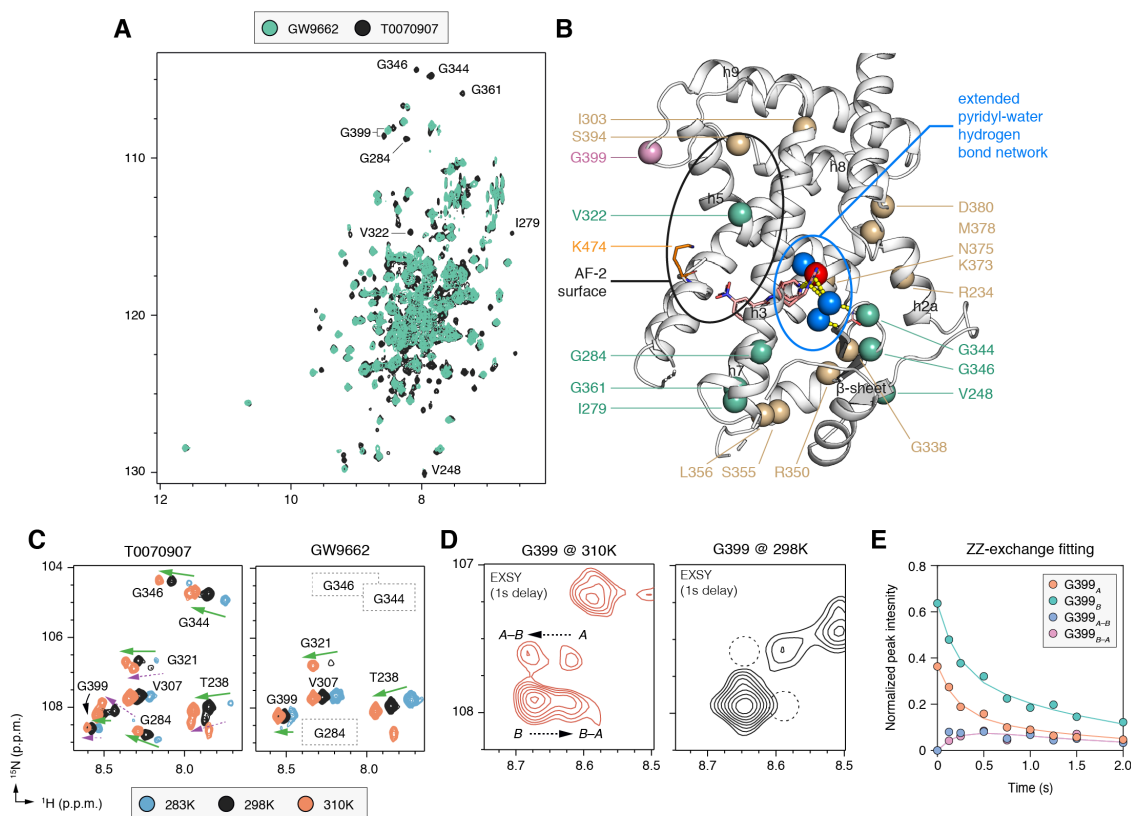
Figure 4. NMR detected exchange between two long-lived T0070907-bound conformations.

(**A**) Overlay of [^{1}H,^{15}N]-TROSY-HSQC NMR spectra of ^{15}N-PPARγ LBD bound to GW9662 or T0070907.

(**B**) Binding of T0070907 but not GW9662 stabilizes intermediate exchange (µs-ms time scale) dynamics (residues labeled in (**A**) shown in green spheres) and causes peak doubling (tan and pink spheres; G399 is colored pink for emphasis). Data plotted on the T0070907-bound PPARγ crystal structure and important structural regions are highlighted as follows: AF-2 surface (black oval); an extended pyridyl-water hydrogen bond network (blue spheres, yellow dotted lines, blue oval), beyond the key pyridyl-water interaction (red sphere).

(**C**) Snapshot overlays of [^{1}H,^{15}N]-TROSY-HSQC spectra of ^{15}N-PPARγ LBD bound to T0070907 or GW9662. The spectral region displayed shows single peaks are observed when bound to either ligand (denoted with green arrows), temperature-dependent NMR peak doubling when bound to T0070907 (purple dotted arrows), and absent peaks due to intermediate exchange on the NMR time scale when bound to GW9662 (dotted rectangles)

(**D**) Snapshots of ZZ-exchange ^{15}N-HSQC NMR spectra (delay = 1 s) of T0070907-bound ^{15}N-PPARγ LBD focused on G399 at the indicated temperatures. Two G399 conformational states are denoted as *A* and *B* with the ZZ-exchange transfer crosspeaks as *A–B* and *B–A*.

(**E**) ZZ-exchange NMR analysis build-up curve from for G399 at 310K generated by plotting peak intensities of the state *A* and *B* peaks and exchange crosspeaks (*A–B* and *B-A*) as a function of delay time.
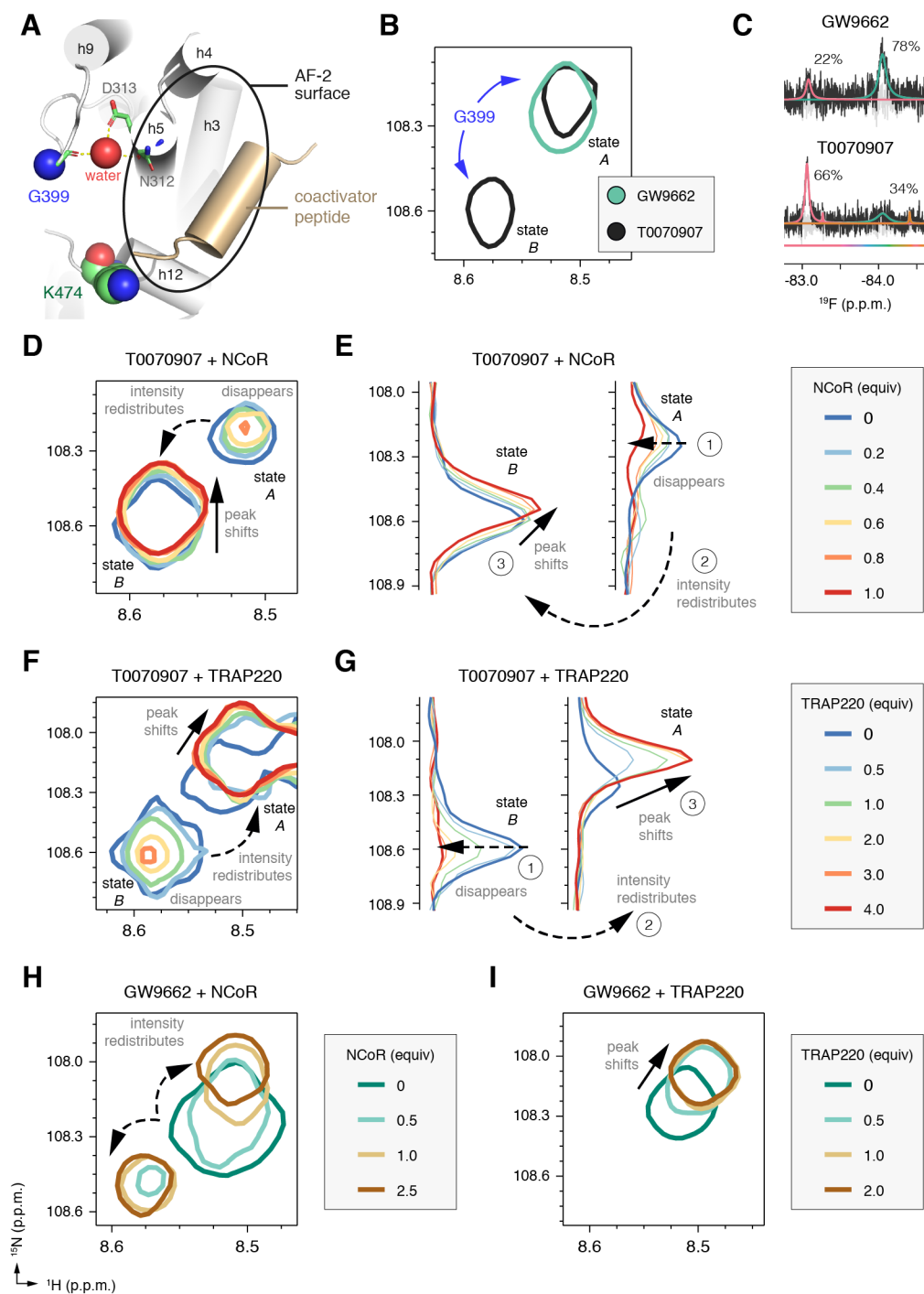
Figure 5. T0070907 but not GW9662 prepopulates a corepressor-bound conformation.

(**A**) Structural location of G399, which is connected to the AF-2 coregulator interaction surface via water-mediated hydrogen bonds to N312 and D313 but does not directly interact with a coregulator peptide bound to the PPARγ LBD (PDB code 2PRG).
(**B**) Snapshot overlay of [¹H,¹⁵N]-TROSY-HSQC NMR spectra of ¹⁵N-PPARγ LBD bound

to GW9662 or T0070907 shows that the single GW9662-bound G399 peak has similar chemical shift values to one of the two T0070907-bound G399 peaks (state A) whereas state B is uniquely populated by T0070907.

(**C**) Deconvoluated ^{19}F NMR data of BTFA-labeled PPARγ LBD covalently bound to GW9662 or T0070907.

(**D–I**) Snapshots of [^{1}H,^{15}N]-TROSY-HSQC spectra of ^{15}N-PPARγ LBD bound to (**D,E**) T0070907 and titrated with NCoR peptide; (**F,G**) T0070907 and titrated with TRAP220 peptide; (**H**) GW9662 and titrated with NCoR peptide; and (**I**) GW9662 and titrated with TRAP220 peptide. 1D spectra in (**E**) and (**G**) show ^{15}N planes extracted from (**D**) and (**F**), respectively, to better illustrate the peak transitions: **1**, disappearance of the state A or B peak; **2**, the redistribution of their intensities to the other state; and **3**, the slight shifting of the other state towards, increased population of, the peptide-bound state.

References

1.   Soccio, R.E., Chen, E.R. & Lazar, M.A. Thiazolidinediones and the promise of insulin sensitization in type 2 diabetes. *Cell Metab* **20**, 573-91 (2014).

2.   Choi, J.H. et al. Anti-diabetic drugs inhibit obesity-linked phosphorylation of PPARgamma by Cdk5. *Nature* **466**, 451-6 (2010).

3.   Choi, J.H. et al. Antidiabetic actions of a non-agonist PPARgamma ligand blocking Cdk5-mediated phosphorylation. *Nature* **477**, 477-81 (2011).

4.   Choi, S.S. et al. A novel non-agonist peroxisome proliferator-activated receptor gamma (PPARgamma) ligand UHC1 blocks PPARgamma phosphorylation by cyclin-dependent kinase 5 (CDK5) and improves insulin sensitivity. *J Biol Chem* **289**, 26618-29 (2014).

5.   Stechschulte, L.A. et al. PPARG Post-translational Modifications Regulate Bone Formation and Bone Resorption. *EBioMedicine* **10**, 174-84 (2016).

6.   Marciano, D.P. et al. Pharmacological repression of PPARgamma promotes osteogenesis. *Nat Commun* **6**, 7443 (2015).

7.   Picard, F. et al. Sirt1 promotes fat mobilization in white adipocytes by repressing PPAR-gamma. *Nature* **429**, 771-6 (2004).

8.   Nakano, R. et al. Antagonism of peroxisome proliferator-activated receptor gamma prevents high-fat diet-induced obesity in vivo. *Biochem Pharmacol* **72**, 42-52 (2006).

9.   Zaytseva, Y.Y., Wallis, N.K., Southard, R.C. & Kilgore, M.W. The PPARgamma antagonist T0070907 suppresses breast cancer cell proliferation and motility via both PPARgamma-dependent and -independent mechanisms. *Anticancer Res* **31**, 813-23 (2011).

10.   Burton, J.D., Goldenberg, D.M. & Blumenthal, R.D. Potential of peroxisome proliferator-activated receptor gamma antagonist compounds as therapeutic agents for a wide range of cancer types. *PPAR Res* **2008**, 494161 (2008).

11.   Nakajima, A. et al. Inhibition of peroxisome proliferator-activated receptor gamma activity suppresses pancreatic cancer cell motility. *Cancer Sci* **99**, 1892-900 (2008).

12.   Johnson, B.A. et al. Ligand-induced stabilization of PPARgamma monitored by NMR spectroscopy: implications for nuclear receptor activation. *J Mol Biol* **298**, 187-94 (2000).

13.   Hughes, T.S. et al. Ligand and receptor dynamics contribute to the mechanism of graded PPARγ agonism. *Structure* **20**, 139-50 (2012).

14.   Bruning, J.B. et al. Partial agonists activate PPARgamma using a helix 12 independent mechanism. *Structure* **15**, 1258-71 (2007).

15.   Berger, J.P. et al. Distinct properties and advantages of a novel peroxisome proliferator-activated protein [gamma] selective modulator. *Mol Endocrinol* **17**, 662-76 (2003).

16.   Trump, R.P. et al. Co-crystal structure guided array synthesis of PPARgamma inverse agonists. *Bioorg Med Chem Lett* **17**, 3916-20 (2007).

17.   Leesnitzer, L.M. et al. Functional consequences of cysteine modification in the ligand binding sites of peroxisome proliferator activated receptors by GW9662. *Biochemistry* **41**, 6640-50 (2002).

18.   Lee, G. et al. T0070907, a selective ligand for peroxisome proliferator-activated receptor gamma, functions as an antagonist of biochemical and cellular activities. *The Journal of biological chemistry* **277**, 19649-57 (2002).

19.   Brust, R. et al. Modification of the Orthosteric PPARγ Covalent Antagonist Scaffold Yields an Improved Dual-Site Allosteric Inhibitor. *ACS Chemical Biology* **12**, 969-978 (2017).

20.   Ge, K. et al. Transcription coactivator TRAP220 is required for PPAR gamma 2-stimulated adipogenesis. *Nature* **417**, 563-7 (2002).

21.   Yu, C. et al. The nuclear receptor corepressors NCoR and SMRT decrease peroxisome proliferator-activated receptor gamma transcriptional activity and repress 3T3-L1 adipogenesis. *J Biol Chem* **280**, 13600-5 (2005).

22.   Liberato, M.V. et al. Medium chain fatty acids are selective peroxisome proliferator activated receptor (PPAR) gamma activators and pan-PPAR partial agonists. *PLoS One* **7**, e36297 (2012).

23.   Evans, B.A., Sato, M., Sarwar, M., Hutchinson, D.S. & Summers, R.J. Ligand-directed signalling at beta-adrenoceptors. *Br J Pharmacol* **159**, 1022-38 (2010).

24.   Kenakin, T. New concepts in pharmacological efficacy at 7TM receptors: IUPHAR review 2. *Br J Pharmacol* **168**, 554-75 (2013).

25.   Kojetin, D.J. & Burris, T.P. Small molecule modulation of nuclear receptor conformational dynamics: implications for function and drug discovery. *Molecular pharmacology* **83**, 1-8 (2013).

26.   Hughes, T.S. et al. An alternate binding site for PPARγ ligands. *Nat Commun* **5**, 3571 (2014).

27.   Kleckner, I.R. & Foster, M.P. An introduction to NMR-based approaches for measuring protein dynamics. *Biochim. Biophys. Acta* **1814**, 942-68 (2011).

28.   Pennington, L.D. & Moustakas, D.T. The Necessary Nitrogen Atom: A Versatile High-Impact Design Element for Multiparameter Optimization. *J Med Chem* **60**, 3552-3579 (2017).

29.   Fujioka, M. & Omori, N. Subtleties in GPCR drug discovery: a medicinal chemistry perspective. *Drug Discov Today* **17**, 1133-8 (2012).

30.   Dosa, P.I. & Amin, E.A. Tactical Approaches to Interconverting GPCR Agonists and Antagonists. *J Med Chem* **59**, 810-40 (2016).

31.   Watson, P.J., Fairall, L. & Schwabe, J.W. Nuclear hormone receptor co-repressors: structure and function. *Mol Cell Endocrinol* **348**, 440-9 (2012).

32.   Einstein, M. et al. The differential interactions of peroxisome proliferator-activated receptor gamma ligands with Tyr473 is a physical basis for their unique biological activities. *Mol Pharmacol* **73**, 62-74 (2008).

33.   Acton, J.J., 3rd et al. Benzoyl 2-methyl indoles as selective PPARgamma modulators. *Bioorg Med Chem Lett* **15**, 357-62 (2005).

34.   Battye, T.G., Kontogiannis, L., Johnson, O., Powell, H.R. & Leslie, A.G. iMOSFLM: a new graphical interface for diffraction-image processing with MOSFLM. *Acta Crystallogr D Biol Crystallogr* **67**, 271-81 (2011).

35.   Winn, M.D. et al. Overview of the CCP4 suite and current developments. *Acta Crystallogr D Biol Crystallogr* **67**, 235-42 (2011).

36.   McCoy, A.J. et al. Phaser crystallographic software. *J Appl Crystallogr* **40**, 658-674 (2007).

37.   Adams, P.D. et al. The Phenix software for automated determination of macromolecular structures. *Methods* **55**, 94-106 (2011).

38.   Nolte, R.T. et al. Ligand binding and co-activator assembly of the peroxisome proliferator-activated receptor-gamma. *Nature* **395**, 137-43 (1998).

39.   Emsley, P. & Cowtan, K. Coot: model-building tools for molecular graphics. *Acta Crystallogr D Biol Crystallogr* **60**, 2126-32 (2004).

40.   Eswar, N. et al. Comparative protein structure modeling using Modeller. *Curr Protoc Bioinformatics* **Chapter 5**, Unit-5 6 (2006).

41.   Pettersen, E.F. et al. UCSF Chimera--a visualization system for exploratory research and analysis. *J Comput Chem* **25**, 1605-12 (2004).

42.   Gordon, J.C. et al. H++: a server for estimating pKas and adding missing hydrogens to macromolecules. *Nucleic Acids Res* **33**, W368-71 (2005).

43.   Vanquelef, E. et al. R.E.D. Server: a web service for deriving RESP and ESP charges and building force field libraries for new molecules and molecular fragments. *Nucleic Acids Res* **39**, W511-7 (2011).

44.   Cornell, W.D., Cieplak, P., Bayly, C.I. & Kollmann, P.A. Application of RESP charges to calculate conformational energies, hydrogen bond energies, and free energies of solvation. *J. Am. Chem. Soc,* **115**, 9620–9631 (1993).

45.   Maier, J.A. et al. ff14SB: Improving the Accuracy of Protein Side Chain and Backbone Parameters from ff99SB. *J Chem Theory Comput* **11**, 3696-713 (2015).

46.   Wang, J., Wolf, R.M., Caldwell, J.W., Kollman, P.A. & Case, D.A. Development and testing of a general amber force field. *J Comput Chem* **25**, 1157-74 (2004).

47.   Hopkins, C.W., Le Grand, S., Walker, R.C. & Roitberg, A.E. Long-Time-Step Molecular Dynamics through Hydrogen Mass Repartitioning. *J Chem Theory Comput* **11**, 1864-74 (2015).

48.   Ryckaert, J.P., Ciccotti, G. & Berendsen, H.J.C. Numerical integration of the cartesian equations of motion of a system with constraints: molecular dynamics of n-alkanes. *J Comput Phys* **23**, 327-41 (1977).

49.   Roe, D.R. & Cheatham, T.E.I. PTRAJ and CPPTRAJ: Software for Processing and Analysis of Molecular Dynamics Trajectory Data. *J Chem Theory Comput* **9**, 3084-95 (2013).

50.   Fabiola, F., Bertram, R., Korostelev, A. & Chapman, M.S. An improved hydrogen bond potential: impact on medium resolution protein structures. *Protein Sci* **11**, 1415-23 (2002).

51.   Greenfield, N.J. Using circular dichroism collected as a function of temperature to determine the thermodynamics of protein unfolding and binding interactions. *Nat Protoc* **1**, 2527-35 (2006).

52.   Johnson, B.A. Using NMRView to visualize and analyze the NMR spectra of macromolecules. *Methods Mol Biol* **278**, 313-52 (2004).

53.   Williamson, M.P. Using chemical shift perturbation to characterise ligand binding. *Prog Nucl Magn Reson Spectrosc* **73**, 1-16 (2013).

54.   Palmer, A.G., 3rd, Kroenke, C.D. & Loria, J.P. Nuclear magnetic resonance methods for quantifying microsecond-to-millisecond motions in biological macromolecules. *Methods Enzymol* **339**, 204-38 (2001).

55.   Gustafson, C.L. et al. A Slow Conformational Switch in the BMAL1 Transactivation Domain Modulates Circadian Rhythms. *Mol Cell* **66**, 447-457 e7 (2017).

56.   Hughes, T.S., Wilson, H.D., de Vera, I.M. & Kojetin, D.J. Deconvolution of Complex 1D NMR Spectra Using Objective Model Selection. *PLoS One* **10**, e0134474 (2015).

Table S1. X-ray data collection and refinement statistics.

	T0070907-PPARγ LBD
Data collection	ALS-BCSB 5.0.1
Space group	C 1 2 1
Cell dimensions	
a, b, c (Å)	92.99, 61.69, 118.66
α, β, γ (°)	90, 102.31, 90
Resolution	45.43–2.26 (2.341–2.26)
R_{pim}	0.02979 (0.3361)
I / σ(I)	10.73 (2.12)
CC1/2 in highest shell	0.906
Completeness (%)	99.53 (99.84)
Redundancy	2.0 (2.0)
Refinement	
Resolution (Å)	2.26
No. of reflections	61110
R_{work}/R_{free} (%)	21.54/28.38
No. of atoms	
Protein	4181
Water	308
B-factors	
Protein	32.35
Ligand	44.64
Water	30.64
Root mean square	
Bond lengths (Å)	0.008
Bond angles (°)	0.94
Ramachandran favored	95.11
Ramachandran outliers	0.59
PDB accession code	6C1I
Values in parentheses indicate highest resolution shell.	
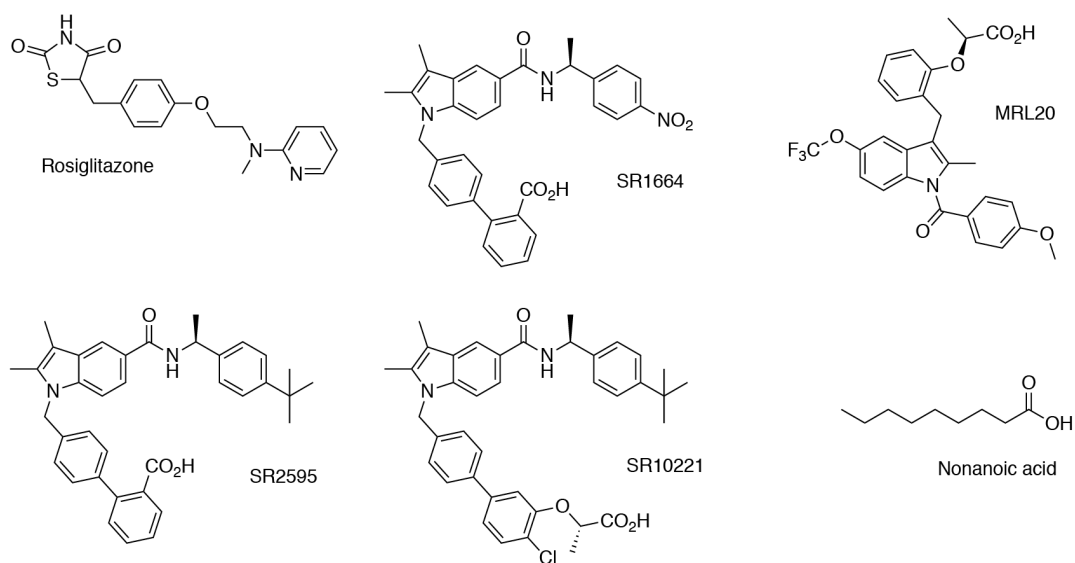
Figure S1. Noncovalent ligands used in the study.
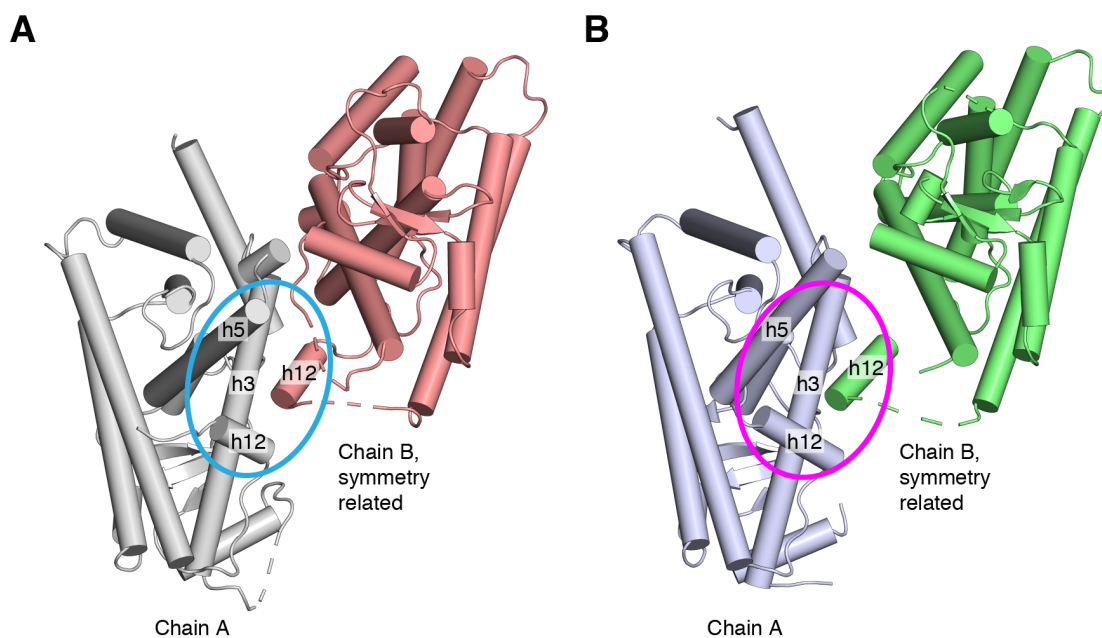
Figure S2. Distorted helix 12 conformations due to crystal contacts.

Shown are chain A and the symmetry related chain B for the (**A**) T0070907-bound and (**B**) GW9662-bound (PDB 3B0R) PPARγ LBD crystal structures, where the chain B helix 12 docks into the AF-2 surface of chain A formed by helix 3, 5, and 12.
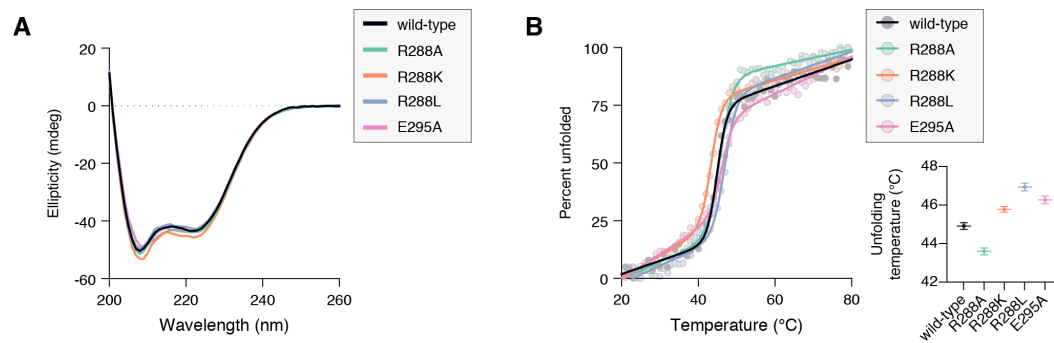
Figure S3. Circular dichroism (CD) spectroscopy data on PPARγ LBD mutants.

(**A**) CD spectra and (**B**) CD thermal melt experiments (inset, fitted melting/unfolding temperatures).

Figure S4. NMR reveals a slow global conformational change between two long-lived conformations with distinct coregulator binding preferences.

Data shown for the residues indicated to the right, which are displayed on the PPARγ LBD structure in **Fig. 4b**. (**A**) Snapshot overlays of ZZ-exchange ^{15}N-HSQC NMR spectra of T0070907-bound ^{15}N-PPARγ LBD; delay = 1 s (red peaks) and 0 s (grey peaks). (**B**) Snapshot overlays of [^{1}H,^{15}N]-TROSY-HSQC NMR spectra of ^{15}N-PPARγ LBD bound to GW9662 (green) or T0070907 (black) shows that the single GW9662-bound G399 peak has similar chemical shift values to one of the two (connected by an orange line) T0070907-bound G399 peaks (state *A*); state *B* is uniquely populated by T0070907. (**C,D**) Snapshots of [^{1}H,^{15}N]-TROSY-HSQC spectra of ^{15}N-PPARγ LBD bound to T0070907 and titrated with (**C**) NCoR or (**D**) TRAP220 peptide.